Atmos. Chem. Phys. Discuss., 13, 18535–18579, 2013
www.atmos-chem-phys-discuss.net/13/18535/2013/
doi:10.5194/acpd-13-18535-2013

Atmospheric Chemistry and Physics Discussions

Vertically resolved aerosol properties by multi wavelengths lidar measurements

M. R. Perrone[1], **F. De Tomasi**[1], **and G. P. Gobbi**[2]

[1]Matematical and Physical Department, Universita' del Salento, 73100 Lecce, Italy
[2]Institute of Atmospheric Sciences and Climate, CNR, Rome, Italy

Received: 30 May 2013 – Accepted: 28 June 2013 – Published: 10 July 2013

Correspondence to: M. R. Perrone (perrone@le.infn.it)

Published by Copernicus Publications on behalf of the European Geosciences Union.

Abstract

A new approach is introduced to characterize the dependence on altitude of the aerosol fine mode radius (R_f) and of the fine mode contribution (η) to the aerosol optical thickness (AOT) by three-wavelength lidar measurements. The introduced approach is based on the graphical method of Gobbi et al. (2007), which was applied to AERONET spectral extinction observations and relies on the combined analysis of the Ångstrom exponent ($å$) and its spectral curvature $\Delta å$. Lidar measurements at 355, 532 and 1064 nm were used in this study to retrieve the vertical profiles of $å$ and $\Delta å$ and to determine the dependence on altitude of R_f and η(532 nm) from the $å$–$\Delta å$ combined analysis. Lidar measurements were performed at the Mathematics and Physics Department of Universita' del Salento, in south eastern Italy. Aerosol from continental Europe, the Atlantic, northern Africa, and the Mediterranean Sea are often advected over south eastern Italy and as a consequence, mixed advection patterns leading to aerosol properties varying with altitude are dominant. The proposed approach was applied to eleven measurement days to demonstrate its feasibility in different aerosol load conditions. The selected-days were characterized by AOTs spanning the 0.23–0.67, 0.15–0.41, and 0.04–0.25 range at 355, 532, and 1064 nm, respectively. Lidar ratios varied within the 28–80, 30–70, and 30–55 sr range at 355, 532, and 1064 nm, respectively, for the high variability of the aerosol optical and microphysical properties. $å$(355 nm, 1064 nm) values retrieved from lidar measurements ranged between 0.12 and 2.5 with mean value ±1 standard deviation equal to 1.4 ± 0.5. $\Delta å$ varied within the −0.10–0.87 range with mean value equal to 0.1±0.4. R_f and η(532 nm) values spanning the 0.02–0.30 µm and the 0.30–0.99 range, respectively were associated to the $å$–$\Delta å$ data points. R_f and η values showed no dependence on the altitude. 72 % of the data points were in the $\Delta å$–$å$ space delimited by the η and R_f curves varying within 0.70–0.95 and 0.15–0.05 µm, respectively for the dominance of fine mode particles in driving the AOT over south eastern Italy. Volume depolarization vertical profiles retrieved from lidar measurements, aerosol products from AERONET sunphotometer measurements

ACPD
13, 18535–18579, 2013

collocated in space and time, the BSC-DREAM model, analytical back trajectories, and satellite images were used to demonstrate the robustness of the proposed method.

1 Introduction

Atmospheric aerosols play a central role in influencing the Earth's climate by direct, indirect, and semi-direct effects. In the attempts to quantify these effects, main difficulties arise from the very high variability in time and space of the aerosol concentration and related physical, optical, and chemical properties. The sensitivity of aerosol direct radiative effects and heating rate (HR) profiles to the vertical distribution of aerosol properties was investigated in a recent paper by one of the authors (Perrone et al., 2012). Sensitivity tests indicated that the uncertainties of the aerosol size distribution and its vertical distribution had a large impact mainly on aerosol HR vertical profiles, both in the solar and the terrestrial domain.

Lidar are nowadays the best devices to retrieve vertical profiles of aerosol extinction (α) and backscattering (β) coefficients. More specifically, Raman lidars based on a tripled Nd:YAG laser are able to provide α and β profiles at different wavelengths. Several numerical approaches were developed in the last years to invert α and β measured at multiple wavelengths to particle parameters (Kolgotin and Muller, 2008 and references therein). In the regularization approach described in Veselovskii et al. (2002) five input optical data (three backscattering and two extinction coefficients, so called $3\beta + 2\alpha$) were needed to retrieve the particle size distribution. A numerical approach for the linear estimation of aerosol bulk properties such as particle volume, effective radius and complex refractive index from three aerosol backscattering and one extinction coefficients (so called $3\beta + \alpha$) was recently developed by Veselovskii et al. (2012), since it would be highly desirable to reduce the number of optical channels in some lidar experiments. Simulation studies with regard to the feasibility of using combined observations from sunphotometer and lidars for microphysical characterization of aerosol particles were reported by Pahlow et al. (2006). Then, a numerical tool was developed

ACPD
13, 18535–18579, 2013

by Chaikovsky et al. (2012) to retrieve vertically resolved aerosol microphysical properties by combining backscattering coefficient measurements at 3 wavelengths and sun sky radiance measurements. This activity was performed in the frame of the European Project Aerosol, Clouds, and Trace gases Research InfraStructure Network (ACTRIS, http://www.actris.net/) with the main aim of integrating sunphotometer and lidar measurements from AERONET (Holben et al., 1998) and the European Aerosol Research LIdar NETwork (EARLINET, Matthias et al., 2004) network, respectively. Gross et al. (2011) used multi-wavelength depolarization and Raman lidar measurements to characterize the optical properties of desert dust, marine aerosols, and biomass-burning aerosol and to determine the changes with the altitude of the aerosol types.

The Ångstrom exponent ($å$) capability to be an indicator of the dominant size of atmospheric aerosols was exploited in this study to characterize the dependence on altitude of the aerosol size distribution from lidar measurements at 3 wavelengths (3 optical channels). The Ångstrom exponent that is calculated from the spectral dependence of the aerosol optical thickness (AOT) is commonly used as a good indicator of the dominant size of the atmospheric particles determining the AOT (e.g. Schuster et al., 2006). Values of $å \leq 1$ indicate size distributions dominated by coarse mode aerosols (radii $\geq 0.5\,\mu m$) that are typically associated with dust and sea salt particles, and values of $å \geq 1.5$ indicate size distributions dominated by fine mode aerosols (radii $< 0.5\,\mu m$) that are usually associated with urban pollution and biomass burning particles. Schuster et al. (2006) pointed out that it was important to consider the wavelength pair used to calculate the Ångstrom exponent when making qualitative assessments about the corresponding aerosol size distribution. They found that $å$ values calculated from longer wavelength pairs (e.g. $\lambda = 670, 870\,\mu m$) were sensitive to the fine mode fraction of aerosols but not the fine mode radius. Conversely, shorter wavelength pairs (e.g. $\lambda = 380, 440\,\mu m$) were sensitive to the fine mode effective radius but not the fine mode fraction. However, $å$ cannot provide information on the relative contribution of coarse and fine mode particles if different aerosol types were present in the air column. Large fine mode particles can have the same $å$ as mix-

ACPD
13, 18535–18579, 2013

tures of coarse mode and small fine mode ones (Gobbi et al., 2007). Some authors investigated how the spectral variation of $å$ can provide further information about the aerosol size distribution. Kaufman (1993) pointed out that negative values of the differences $\Delta å = å(440\,\text{nm}, 613\,\text{nm}) - å(440\,\text{nm}, 1003\,\text{nm})$ indicated the dominance of fine mode aerosol, while positive differences indicated the effect of two separate modes with a significant coarse mode contribution. Schuster et al. (2006) addressed the link between the Ångstrom coefficient curvature ($\Delta å/\mathrm{d}\lambda$) and the ratio of fine to total aerosol volume and showed that the spectral variation of $å$ can provide additional information about the aerosol size distribution, as it was summarized in Gobbi et al. (2007). A simple graphical method to visually convert $å$ and its spectral curvature ($\Delta å$) to both the fine mode aerosol radius and the contribution of the fine mode aerosol to the AOT was proposed by Gobbi et al. (2007). In particular, aerosols were classified in a new space $\Delta å$ versus $å$ which was invariant to changes in AOT for a given size distribution. Quality-assured direct-sun data in the 440–870 nm wavelength range retrieved from sun photometers operating within AERONET were used by Gobbi et al. (2007) to demonstrate the feasibility of the introduced classification scheme. Considering the operating wavelengths of AERONET sun photometers, $å$ was derived for the wavelength pairs of 440–870 nm and its spectral curvature was represented by the difference $\Delta å = å(440, 675) - å(675, 870)$. The graphical method was applied by Gobbi et al. (2007) to the analysis of yearly records at 8 sites in 3 continents, characterized by different levels of pollution, biomass burning and mineral dust concentrations. Results depicted the dominance of fine mode aerosols in driving the AOT at polluted sites. Basart et al. (2009) provided an atmospheric aerosol characterization for the North Africa, north eastern Atlantic, Mediterranean and Middle East by applying the $\Delta å$ versus $å$ graphical method to direct sun observations of 39 AERONET stations.

Lidar measurements at 355, 532 and 1064 nm were used in this study to retrieve vertical profiles of $å$ and its spectral curvature $\Delta å$, with the aim of demonstrating the feasibility of the $\Delta å$–$å$ graphical method to characterize the dependence on altitude of the fine mode aerosol radius and the fine mode contribution to the AOT, when atmo-

ACPD
13, 18535–18579, 2013

spheric particles from different sources and hence, of different type were present along the aerosol column. Depolarization lidar measurements, analytical backtrajectory pathways, the BSC-DREAM model (www.bsc.es), satellite images, and AERONET sunphotometer measurements collocated in space and time with lidar measurements were used to identify the presence of different aerosol types in the air column. A short version of the paper was presented at the 9th International Symposium on Tropospheric Profiling (Cavalieri et al., 2012). An overview of the 3 wavelength lidar system and measurements is provided in Sect. 2. The used aerosol classification framework is discussed in Sect. 3. Then, some study cases are presented and discussed in detail in Sect. 4. Results referring to 11 measurements days with different aerosol types in the air column are presented in Sect. 5. Summary and conclusion are given in Sect. 6.

2 Lidar system and measurements

2.1 Description of the lidar system

The ground-based lidar system operating at the Mathematics and Physics Department of Universita' del Salento (Lecce) in south eastern Italy (40.33° N; 18.11° E) and identified as UNILE (UNIversity of LEcce) lidar was used in this study. The UNILE lidar activity is carried out within EARLINET since May 2000. The UNILE lidar system is nowadays composed by a Nd:YAG laser operating at its fundamental wavelength, 1064 nm, and the second and third harmonic at 532 and 355 nm, respectively at a repetition rate of 30 Hz. The linear polarized laser pulses are about 10 ns long. The maximum energy per pulse is 1000 mJ, 150 mJ and 300 mJ, at 1064, 532, and 355 nm, respectively. The 3-wavelength laser beams delivered by the Nd:YAG laser which are spatially separated, are recombined in one beam by dichroic mirrors and sent in the atmosphere by means of a mirror located on the axis of a f/4 Newton telescope. The backscattered radiation collected by the primary mirror of the Newton telescope and collimated by a plano convex lens, is spectrally resolved by means of dichroic mirrors and interfer-

ACPD
13, 18535–18579, 2013

ential filters. Then, the 1064 nm signal is detected by an avalanche photodiode and an A/D transient recorder. The signal at 532 and 355 nm are detected by photomultipliers connected to transient recorders that have both a 12 bit A/D conversion and a photon counting (PC) capability. In this way the full dynamic range of the lidar signals can be monitored. Transient recorders integrate over 2000 laser shots that correspond to about 60 s. The lidar system is estimated to achieve full overlap between 0.5–1.0 km above the ground level (a.g.l.).

2.2 Aerosol parameters from lidar measurements

The UNILE lidar system was designed to derive vertical profiles of the aerosol backscattering ($\beta(z)$) coefficient at 355 nm, 532 nm and 1064 nm, respectively and of the volume depolarization ratio ($\delta(z)$) at 355 nm during day time measurements. Backscattering lidar measurements suffer from a need to assume an aerosol-to-backscatter ratio LR (also referred to as the aerosol-lidar ratio) to solve the ill-posed problem of the lidar equation and extract aerosol extinction and backscattering coefficient profiles. Altitude independent lidar ratios were used in this study to retrieve $\beta(z)$ profiles. A discussion on this assumption is reported in Sect. "Sensitivity test on the lidar ratio vertical profile for 28 July 2011". The extinction coefficient ($\alpha(z)$) profiles were calculated from $\beta(z)$ in accordance with the following relationship $\alpha(z) = \mathrm{LR} \times \beta(z)$. Note that LR values were chosen in order to obtain aerosol optical depths, calculated from the extinction profiles, equal (within ±0.01) to the corresponding ones retrieved from sun photometer measurements collocated in space and time with lidar measurements. More specifically, AOTs were calculated from $\alpha(z)$ profiles by assuming that $\alpha(z)$ values did not vary with altitude below the height where the lidar system was estimated to achieve full overlap. As mentioned in the previous section, the full overlap height is achieved within 0.5–1.0 km a.g.l. This height is of the order of the planetary boundary layer (PBL) height at the monitoring site of this study (De Tomasi and Perrone, 2006; De Tomasi et al., 2011). So, we assumed that aerosol particles were well mixed within the PBL. An AERONET sun/sky photometer operates at the UNILE lidar site

ACPD
13, 18535–18579, 2013

since the year 2003. AERONET provides AOTs with accuracy of ±0.01, according to Dubovik et al. (2002). The statistical uncertainties of $\alpha(z)$ were calculated from the law of error propagation by assuming a Poisson noise on the lidar signals (De Tomasi and Perrone, 2003; De Tomasi et al., 2006). Extinction coefficients with relative statistical uncertainties $\geq 10\,\%$ for $\alpha(z) \geq 10^{-2}\,\mathrm{km}^{-1}$ were rejected. Extinction coefficients lower than $10^{-2}\,\mathrm{km}^{-1}$ and with uncertainties $< 0.5 \times 10^{-2}\,\mathrm{km}^{-1}$ were retained. The volume depolarization ratio profile $\delta(z)$ was calculated from the ratio of the cross-polarized to the parallel-polarized backscattering coefficient and under our experimental conditions it takes the value of 0.0045 in a pure molecular atmosphere and higher values in presence of non spherical particles as desert dust particles. Ångstrom coefficients at the altitude z were calculated as follows:

$$\mathring{a}_{\lambda 1,\lambda 2}(z) = -\{\ln[\alpha_{\lambda 1}(z)/\alpha_{\lambda 2}(z)]\}/[\ln(\lambda 1/\lambda 2)] \quad (1)$$

where $\alpha_{\lambda 1}(z)$ and $\alpha_{\lambda 2}(z)$ represent the extinction coefficient at the height z and at the wavelength $\lambda 1$ and $\lambda 2$, respectively. $\alpha_{\lambda 1}(z)$ and $\alpha_{\lambda 2}(z)$ were calculated from the following relationship:

$$\alpha_{\lambda i}(z) = \mathrm{LR}_{\lambda i} \times \beta_{\lambda i}(z) \quad i = 1,2 \quad (2)$$

where $\mathrm{LR}_{\lambda i}$ and $\beta_{\lambda i}(z)$ represent the lidar ratio and the backscattering coefficient at the wavelength λi, respectively. The statistical uncertainties of $\mathring{a}_{\lambda 1,\lambda 2}(z)$ were calculated from the law of error propagation. Ångstrom coefficients with relative statistical uncertainties $> 20\,\%$ for $|\mathring{a}| \geq 0.1$ were rejected. Ångstrom coefficients lower than 0.1 in absolute value and with uncertainties < 0.02 were retained. The spectral curvature is represented in this study by the difference

$$\Delta\mathring{a}(z) = \mathring{a}_{355,532}(z) - \mathring{a}_{532,1064}(z) \quad (3)$$

The statistical uncertainties of $\Delta\mathring{a}(z)$ were calculated from the law of error propagation.

ACPD
13, 18535–18579, 2013

3 Graphical framework for the aerosol classification

To classify aerosol properties by the $\Delta\mathring{a}(z)$ versus $\mathring{a}_{355,1064}(z)$ scatterplot, reference points corresponding to bimodal size distributions characterized by a variety of fine mode (R_f) and coarse mode (R_c) modal radii combined in order to lead to prescribed fine mode fractions (η) at 532 nm were determined, according to Gobbi et al. (2007). More specifically, Mie calculations of the aerosol spectral extinction for selected R_f (0.02, 0.05, 0.1, 0.15, 0.2, 0.3, and 0.4 µm) and R_c (0.5, 0.6, 0.7, and 0.8 µm) values combined in order to provide η fractions of 1, 10, 30, 50, 70, 90, 99 %, were performed. The real (n) and imaginary (k) refractive index values at 532 nm used in the Mie calculations are given in Table 1. The daily mean values of n and k retrieved from sunphotometer AERONET measurements performed at the monitoring site of this study from 2003 to 2010 yr were used to calculate the mean refractive index values reported in Table 1. More specifically, the Level 2, Quality-Assured values of n and k at 440, 675, and 1018 nm, respectively were used to determine the mean value of n and k at 532 nm reported in Table 1. Figure 1 (black lines) shows the aerosol classification framework calculated by using $n = 1.455$ and $k = 0.0047$ at 532 nm (Table 1). Solid and dashed black lines were calculated for fixed R_f values and for fixed fine mode fraction contributions to the total AOT at 532 nm, respectively. Figure 1 reveals that aerosol size distributions characterized by different values of the fine mode radius and the fine mode fractions can have the same $\mathring{a}_{355,1064}$ and as a consequence, it highlights the aerosol classification framework potential.

Aerosol loads affected by Sahara dust intrusions have frequently been observed at the monitoring site of this study and characterized in a series of papers as Perrone and Bergamo (2011); Santese et al. (2008); Barnaba et al. (2004); De Tomasi et al. (2003). It was also shown that Ångstrom coefficients retrieved from AERONET sunphotometer measurements provided a useful tool to identify dust intrusion events (e.g. Santese et al., 2008). So, daily mean values of $\mathring{a}_{440,675}(z) < 0.5$ were used in this study to identify from 2003 to 2010 years, the AERONET measurement days significantly affected

ACPD
13, 18535–18579, 2013

by dust intrusion events (Perrone and Bergamo, 2011). Then, the AERONET n and k values (Level 2, Quality-Assured-Data) retrieved during the dust affected days were used to define the mean value of the dust affected real (n_c) and imaginary (k_c) refractive index. n_c and k_c values at 532 nm are reported in Table 1 in addition to the mean value of the real (n_f) and the imaginary (k_f) refractive index found by selecting the AERONET measurements days with $\mathring{a}_{440,675}(z) > 1.2$, from 2003 to 2010 years. These last measurements days were considered as characterized by continental pollution, according to Santese et al. (2008). The relative differences of n_c and n_f with n (Table 1) are smaller than 2 % at 532 nm. While, the relative differences of k_c and k_f with k (Table 1) are smaller than 50 %. To this end, it is worth mentioning that according to Dubovik et al. (2002), the expected accuracy for the real part of the refractive index is of 0.04 for AOT(440 nm) $\geq$ 0.5 and of 0.05 for AOT(440 nm) $\leq$ 0.2. The values of the imaginary part of the refractive index are instead retrieved with errors of the order of 30–50 % for AOT(440 nm) $\geq$ 0.5 and of the order of 80–100 % for AOT(440 nm) $\leq$ 0.2. Red and blue lines in Fig. 1 represent the aerosol classification framework calculated by using the refractive index values for dust (n_c, k_c) and pollution (n_f, k_f) affected days, respectively (Table 2) and highlight the dependence of the graphical framework on refractive index values. Figure 1 shows a clockwise rotation about the origin of the constant radius curves as the real part of the refractive index increases from 1.445 to 1.483 and the imaginary part increases from 0.0035 to 0.0070. The maximum R_f indetermination generated by this range of refractive indexes is of the order of ±30 % for $R_f \geq 0.05$ µm. While, the maximum indetermination of η is of the order of ±5 % for $\eta \leq 90$ %.

4 Analysis of case studies

Some case studies are analyzed in this section to demonstrate the robustness of the proposed graphical method and characterize the dependence on altitude of the fine mode aerosol contribution and the fine mode aerosol radius on the basis of lidar measurements of $\mathring{a}$ and $\Delta\mathring{a}$.

ACPD
13, 18535–18579, 2013

4.1 Case Study: 28 July 2011

Figure 2a shows the extinction coefficient profiles at 355 nm (black line), 532 nm (green line), and 1064 nm (red line) retrieved from lidar measurements performed on 28 July 2011 from 12:29 to 13:00 UTC. $\alpha(z)$ statistical uncertainties are not plotted to make the figure more clear. The altitude independent lidar ratio value was equal to 80 sr, 70 sr, and 50 sr at 355 nm, 532 nm, and 1064 nm, respectively. Selected LR values and AOTs calculated from the extinction coefficient profiles are reported in Table 2. AOTs were in accordance within ±0.1 with the corresponding values retrieved from the AERONET (Lecce University) sunphotometer measurements at 12:55 UTC. Level 1.5 AERONET products were used since Level 2 products were not available. The AOT at 675 nm, the columnar fine mode fraction (η) at 675 nm, the fine mode median radius (R_f), $\mathring{a}_{440,870}$ and $\Delta\mathring{a} = \mathring{a}_{440,675} - \mathring{a}_{675,870}$ retrieved from AERONET sunphotometer measurements performed at the time T_A = 12:55 UTC are also given in Table 2 for comparison. Aerosol particles up to ∼ 5 km a.g.l. were detected by the lidar on 28 July. In particular, the particles located within about 3–5 km a.g.l. were responsible for rather large extinction coefficients at 355 and 532 nm, respectively. The blue line in Fig. 2c represents the volume-depolarization-ratio profile. $\delta(z)$ values decrease with the increase of the altitude and are smaller than 0.7 % within 3.2–4.8 km a.g.l. The vertical profiles of the Ångstrom coefficients $\mathring{a}_{355,532}(z)$, $\mathring{a}_{532,1064}(z)$, $\mathring{a}_{355,1064}(z)$, and of the spectral curvature $\Delta\mathring{a}(z)$ are plotted in Fig. 2b. $\mathring{a}(z)$ and $\Delta\mathring{a}(z)$ values retrieved at $z \geq 1$ km a.g.l. are only reported in Fig. 2b, since the lidar system is estimated to achieve full overlap at $z \geq 1$ km a.g.l. $\mathring{a}$ values vary with altitude and the trend is similar for all wavelength pairs. In particular, $\mathring{a}_{355,1064}(z)$ increases from ∼ 0 to 2.5 within 1.2–4.8 km a.g.l. $\Delta\mathring{a}$ varies from −1 to 1 within the same altitude range. The change with the altitude of the aerosol size distribution and hence of the aerosol type was responsible for the dependence of $\mathring{a}$ and $\Delta\mathring{a}$ on z. Ångstrom coefficients and volume depolarization ratio profiles indicate that the contribution of fine ($\mathring{a} > 1.5$), spherical particle ($\delta(z) < 1.0$ %) was rather large within 3.2–4.8 km a.g.l. Conversely, the $\delta(z)$ and $\mathring{a}(z)$ values found

ACPD
13, 18535–18579, 2013

within the 1–3 km range a.g.l. indicate that the contribution of coarse, non-spherical particles was larger within this last altitude range. Calculated $\Delta\mathring{a}(z)$ versus $\mathring{a}(z)$ values are plotted in Fig. 3a (open dots). Error bars represent ±1 standard deviation (SD) of the mean value. Different colours were used to represent $\Delta\mathring{a}(z)$–$\mathring{a}(z)$ values referring to different z, as indicated by the colour bar on the top of Fig. 3a. The graphical framework calculated for $n = 1.455$ and $k = 0.0047$ at 532 nm is shown in Fig. 3a. These refractive index values were considered representative of aerosol loads affected by mixed aerosol types, in accordance with the discussion reported in the previous section. Figure 3 (open dots) shows that the $\mathring{a}$–$\Delta\mathring{a}$ data points within 1–2 km a.g.l. correspond to $\eta(z)$ values varying within the 0.3–0.7 range and $R_f(z)$ values spanning the 0.07–0.20 µm range. Conversely, the aerosol load located within 3.2–4.8 km a.g.l. was characterized by $\eta(z)$ values spanning the 0.90–0.99 range and $R_f(z)$ varying within about 0.02–0.18 µm. These results indicate that the contribution of fine mode particles progressively increased with the altitude while, the fine mode radius decreased with the altitude. Hence, the aerosol size distribution varied significantly with the altitude on 28 July 2011.

Analytical back trajectories from the Hybrid Single Particle Lagrangian Integrated Trajectory Model (HYSPLIT) (Draxler and Rolph, 2003) were used to know about the source regions of the air masses advected over south eastern Italy on 28 July 2011 and to understand and support the $\eta(z)$ and $R_f(z)$ values retrieved from the $\Delta\mathring{a}(z)$–$\mathring{a}(z)$ scatterplot. Figure 4a shows the pathways estimated at 13:00 UTC of the ten day backtrajectories with arrival heights at 1, 2, and 4 km a.g.l. The time evolution of the altitude of each backtrajectory is plotted in Fig. 4b. Northern America was the source region of the air masses arriving from 1 up to 4 km a.g.l. Nevertheless, it is worth noting that the air masses at 2 km arrival height crossed Northern Africa at low altitudes before reaching south eastern Italy and as a consequence, they were likely responsible for the transport of desert dust particles. Volume depolarization ratio measurements support last comment (Fig. 2c). The BSC-DREAM model also supports the advection of Sahara dust particles over south eastern Italy. It simulated for the monitoring site

ACPD
13, 18535–18579, 2013

of this study, the existence of a dust layer centred around 1.7 km at 12:00 UTC. Figure 2c (red line) shows the vertical profile of the dust particle concentration from the BSC-DREAM model (http://www.bsc.es/earth-sciences/mineral-dust-forecast-system/bsc-dream8b-forecast/north-africa-europe-and-middle-ea-0) and the volume depolarization ratio profile (blue line) at 355 nm retrieved from lidar measurements. It is interesting to observe that the extinction coefficients (Fig. 2a) and $\delta(z)$ reach a peak value at ∼ 2 and ∼ 1.7 km a.g.l., respectively where the dust particle concentration also reaches largest values (Fig. 2c). Hence, the $\eta(z)$ and $R_f(z)$ values that span the 0.3–0.7 and 0.07–0.20 µm range, respectively within ∼ 1–2.5 km a.g.l., were likely due to the contribution of desert dust particles. Conversely, the $\eta(z)$ and $R_f(z)$ values within 3.2–4.8 km a.g.l. which vary from 0.90 to 0.99 and from 0.02 µm to 0.18 µm, respectively were likely due to anthropogenic pollution from Northern America, in accordance with Fig. 4. Typical size distribution associated to desert dust and continental pollution support last comments (Seinfeld and Pandis, 1998).

The black box in Fig. 3a represents the columnar $\Delta\mathring{a}_{in}$ and $\mathring{a}_{in}(355, 1064)$ values calculated from the AOTs at 355, 532, and 1064 nm by using the following relationships:

$$\mathring{a}_{in}(\lambda_1, \lambda_2) = -[\ln(AOT_{\lambda 1}/AOT_{\lambda 2})]/[\ln(\lambda_1/\lambda_2)] \quad (4)$$

$$\Delta\mathring{a}_{in} = \mathring{a}_{in}(355, 532) - \mathring{a}_{in}(532, 1064) \quad (5)$$

We found $\Delta\mathring{a}_{in} = -0.09$ and $\mathring{a}_{in}(355, 1064) = 1.5$ in satisfactory agreement with the $\mathring{a}_{448,870}$, and $\Delta\mathring{a} = \mathring{a}_{448,675} - \mathring{a}_{675,870}$ values retrieved from AERONET sunphotometer measurements (Table 2). $\mathring{a}_{in} - \Delta\mathring{a}_{in}$ values correspond to $\eta_{in} \cong 0.9$ and $R_{f-in} \cong 0.12$ µm which can be considered typical of continental pollution (Seinfeld and Pandis, 1998). This result highlights the differences which may occur between vertical-resolved and column-integrated η and R_f values. In particular, Fig. 3 shows that the $\Delta\mathring{a}_{in} - \mathring{a}_{in}$ data point (black box) leads to the underestimation of $\eta(z)$ and the overestimation of $R_f(z)$ at $z > 3$ km, and to the overestimation of $\eta(z)$ and the underestimation of $R_f(z)$ at $z < 2$ km. The differences between vertical-resolved and column-integrated η and R_f values are expected to be quite large when aerosol of different type/origin are located at differ-

ACPD
13, 18535–18579, 2013

ent altitudes, as occurred in the study case of this section. Note that aerosols from continental Europe, the Atlantic and Mediterranean Sea, and African deserts are frequently advected over the monitoring site of this study and more generally all over the Central Mediterranean, as the case study of this section has revealed. As a consequence, aerosol size distributions may significantly vary with the altitude over the Central Mediterranean and this must be accounted for in radiative transfer simulations (Perrone et al., 2012).

Sensitivity test on the lidar ratio vertical profile for 28 July 2011

The results presented in the previous section have revealed that the aerosol size distribution may significantly vary with altitude when aerosols of different type (origin) are located at different altitudes. Measurements and model data have revealed that the aerosol particles within 1–2.5 km a.g.l. were quite affected by Saharan dust on 28 July 2011. On the contrary, it was found that fine mode particles, likely due to continental pollution, were prevailing within 3.2–4.8 km a.g.l. Lidar ratios values depend on aerosol optical and microphysical properties and as a consequence, they vary with the aerosol type. Thus, the use in the previous section of an altitude independent lidar ratio value to retrieve the extinction lidar profiles at 355, 532, and 1064 nm represents a weak point of the performed analysis. Lidar ratio values dependent on altitude are used in this section to test the sensitivity on lidar ratios of $\Delta\mathring{a}(z)$ and $\mathring{a}_{355,1064}(z)$ and of the corresponding $\eta(z)$ and $R_f(z)$ values for the case study of 28 July 2011. More specifically, lidar ratios equal to 88 sr, 75 sr, and 55 sr at 355 nm, 532 nm, and 1064 nm, respectively were used at 2.5 km $\leq z \leq$ 5 km a.g.l. These values are 10 % higher than the column independent lidar ratios used in the previous section. Note that lidar ratio values at 351 nm even larger than 100 sr were retrieved over south eastern Italy during the advection of continental pollution, according to Barnaba et al. (2007). Lidar ratios equal to 55 sr, 55 sr and 50 sr at 355 nm, 532 nm, and 1064 nm, respectively were instead used at $z <$ 2.5 km, where the contribution of desert dust particles was larger. LRs at 351 nm spanning on average the 60–50 sr range were retrieved over

ACPD
13, 18535–18579, 2013

south eastern Italy during the advection of desert dust particles (e.g. De Tomasi et al., 2003; Barnaba et al., 2004). It is also well known that LRs for desert dust particles are weakly dependent on wavelength (e.g. Tesche et al., 2009). The above selected LRs have allowed obtaining AOTs in accordance within ±0.1 with the corresponding values retrieved from the AERONET sunphotometer measurements at 12:55 UTC. Figure 2d shows the vertical profiles of $\Delta\mathring{a}(z)$ and $\mathring{a}_{355,1064}(z)$ retrieved from the altitude-dependent LRs. The dotted lines in Fig. 2d show for comparison the vertical profile of $\Delta\mathring{a}(z)$ and $\mathring{a}_{355,1064}(z)$ retrieved from the altitude independent LRs. The differences between the solid and dotted lines increase at $z < 2.5$ km, since the LRs at 355 nm and 532 nm were 25 % and 21 % smaller, respectively than the corresponding column independent LRs used within 1–2.5 km a.g.l. Figure 3b shows $\Delta\mathring{a}(z)$ versus $\mathring{a}_{355,1064}(z)$. The comparison of Fig. 3b (open triangles) with Fig. 3a (open dots) reveals that the 10 % increase of LR values at $z \geq 2.5$ km has not significantly affected the $\Delta\mathring{a}(z)$ versus $\mathring{a}_{355,1064}(z)$ plot and as a consequence, the corresponding $\eta(z)$ and $R_f(z)$ values. On the contrary, the use of smaller LRs at $z < 2.5$ km has been responsible for the decrease of both the $\eta(z)$ and $R_f(z)$ values. These last results indicate that LR values larger than the ones commonly used for dust affected aerosol loads may be responsible for the overestimation of both the aerosol fine mode fraction and the fine mode radius. Hence, LR values varying with the altitude must be used when aerosol of different type and characterized by different LR values are located at different altitudes a.g.l. However, it is worth noting that we have found that $\eta(z)$ and $R_f(z)$ values were not significantly affected by the 10 % increase of LR values.

The following methodology is suggested to select altitude-dependent lidar ratios, in accordance with the above reported analysis. Altitude-independent LRs could at first been used to obtain a first guess on the $\Delta\mathring{a}(z)$ and $\mathring{a}_{355,1064}(z)$ profiles and corresponding $\eta(z)$ and $R_f(z)$ values. Then, if the proposed graphical approach combined with backtrajectories and model data will allow inferring the dependence on z of the main aerosol types and hence of the prevailing lidar ratios values, it would be preferable to re-calculate $\Delta\mathring{a}(z)$ and $\mathring{a}_{355,1064}(z)$ profiles from extinction profiles based on

ACPD
13, 18535–18579, 2013

altitude dependent LRs, to reduce the uncertainties on $\eta(z)$ and $R_f(z)$ values. However, it is worth mentioning that the uncertainty in choosing the lidar ratio value can be large, since LRs depend on the source regions of the aerosol particles and on the pathways the aerosols crossed before reaching the monitoring site (e.g. Barnaba et al., 2004, 2007; De Tomasi et al., 2006). The coexistence in a layer of different aerosol types can also give rise to considerable uncertainty in choosing the lidar ratio value. So, we decided to use altitude independent LRs in the case studies analyzed in this paper. We believe that the uncertainties on the $\eta(z)$ and $R_f(z)$ values due to the assumption of an altitude independent LR would be comparable, in most of the case studies, to the ones resulting from an inappropriate choice of the LR value, as a consequence of the addressed problems. In conclusion, we believe that the assumption on lidar ratios has not significantly affected the main purpose of this study which was to demonstrate the applicability of the proposed approach.

4.2 Case study: 29 August 2011

Lidar measurements performed at different day hours of 29 August 2011 were analyzed in this case study to test the capability of the proposed graphical method to determine changes with time and altitude of η and R_f values. Figure 5a shows the extinction coefficient profile at 355 nm (blue line), 532 nm (green line), and 1064 nm (red line) retrieved from lidar measurements performed on 29 August 2011 from 11:44 to 12:17 UTC. The altitude independent lidar ratio value was equal to 55 sr, 50 sr, and 38 sr at 355 nm, 532 nm, and 1064 nm, respectively. Selected LR values and calculated AOTs are in Table 2. AOTs were in accordance within ±0.1 with the corresponding ones retrieved from the AERONET sunphotometer measurements at 11:51 UTC. Aerosol particles up to ∼ 4 km a.g.l. were detected by the lidar. The blue line in Fig. 5a shows the vertical profile of the volume depolarization ratio. $\delta(z)$ is $\cong 2\,\%$ within 1.5–3.2 km a.g.l. and takes smaller values at lower altitudes. This last result indicates that the contribution of non spherical particles was larger within 1.5–3.2 km a.g.l. Figure 5b shows the vertical profiles of $\mathring{a}_{355,532}(z)$, $\mathring{a}_{532,1064}(z)$, and $\mathring{a}_{355,1064}(z)$ and of the spectral cur-

ACPD
13, 18535–18579, 2013

vature $\Delta\mathring{a}(z) = \mathring{a}_{355,532}(z) - \mathring{a}_{532,1064}(z)$. We observe that $\mathring{a}_{355,532}(z)$ spans the 0.9–1.7 range and increases with the altitude above 1.5 km a.g.l. while, $\mathring{a}_{355,1064}(z)$ is characterized by a weaker dependence on z. $\Delta\mathring{a}(z)$ takes negative values and increases with z at $z \geq 1.5$ km a.g.l. Open dots and error bars in Fig. 6 show the scatterplot of $\Delta\mathring{a}(z)$ versus $\mathring{a}_{355,1064}(z)$. Different colours represent different altitudes in accordance with the colour bar on the top of Fig. 6. A portion of the graphical framework calculated for $n = 1.455$ and $k = 0.0047$ at 532 nm was reported in Fig. 6 to better show the dependence on altitude of the $\mathring{a}(z)$–$\Delta\mathring{a}(z)$ data points ±1 SD. Figure 6 reveals that the $\mathring{a}$–$\Delta\mathring{a}$ data points within 1–2 km a.g.l. correspond to fine mode fraction and fine mode radius values varying within the 0.90–0.99 and the 0.13–0.16 µm range, respectively. While, the $\mathring{a}$–$\Delta\mathring{a}$ data points at altitudes larger than 2.5 km a.g.l. correspond to η values that span the 0.80–0.90 range and R_f values varying within 0.05–0.13 µm. These results indicate that fine mode particles were prevailing on 29 August. However, the size distribution of the aerosol particles located at $z > 2.5$ km a.g.l. was characterized by a smaller fine mode radius and fine mode fraction than the particles located at $z < 2.5$ km. HYSPLIT analytical back trajectories were used to know about the source regions of the air masses advected over south eastern Italy on 29 August 2011 and to understand and support the changes with z of the aerosol microphysical properties revealed by Fig. 6. Figure 7a shows the pathways estimated at 12:00 UTC of the ten-day backtrajectories with arrival heights at 1, 2, and 3 km a.g.l. The time evolution of the altitude of each backtrajectory is plotted in Fig. 7b. Air masses from north-eastern Europe were advected to south eastern Italy on 29 August. Advection patterns similar to the one of Fig. 7a are rather frequent over south eastern Italy mainly in summer, according to Perrone et al. (2013) and Santese et al. (2008). It was also shown by Perrone et al. (2013) that the air flows from northeastern Europe were mainly responsible for the advection of fine mode particles as those due to ammonium sulfate (Fig. 6b of the paper), traffic (Fig. 6f of the paper), and combustion including biomass burning (Fig. 7a of the paper) sources. Lelieveld et al. (2002) also revealed the important contribution of fine pollution aerosols transported from Central and

ACPD
13, 18535–18579, 2013

Eastern Europe to south eastern Italy, in satisfactory agreement with the results from Fig. 6 (open dots). It is worth noting from Fig. 7b that the 1, 2, and 3 km-arrival-height backtrajectories were close to the ground level over Eastern Europe and as a consequence, they were likely responsible for the lifting of soil particles up ∼ 3 km a.g.l. In addition, the true colour image from the Moderate Resolution Imaging Spectroradiometer (MODIS) on board the Aqua satellite revealed the presence of a thin layer of Africa dust particles over south eastern Italy at 12:00 UTC of 29 August 2011 (http://lance-modis.eosdis.nasa.gov/cgi-bin/imagery/single.cgi?granule=A112411200). The BSC-DREAM model also simulated for Lecce the existence of a thin dust layer located within 2–4 km at 12:00 UTC. Note that dust outbreaks and the lack of rainy days mainly occurring in summer over southern Europe, on average enhance the natural and anthropogenic dust resuspension. So, resuspended soil and/or desert dust particles have likely been responsible for the volume depolarization ratios revealed by Fig. 5a (blue line) and the decrease of $\eta(z)$ at larger altitudes revealed by Fig. 6. We believe that the above comments support and allow obtaining a satisfactory understanding of the dependence on altitude of the R_f and η values (Fig. 6, open dots). The black open dot in Fig. 6 represents $\mathring{a}_{in}(355, 1064) = 1.5$ and $\Delta\mathring{a}_{in} = 0.08$, which have been calculated in accordance with Eqs. (4) and (5), respectively, and corresponds to $\eta_{in} \cong 0.8$ and $R_{f-in} \cong 0.08$ µm. Note that the $\mathring{a}$–$\Delta\mathring{a}$ data points of Fig. 6 (open dots) are less spread than the ones of Fig. 3. As a consequence, the differences between $R_f(z)$ and R_{f-in} and $\eta(z)$ and η_{in} are smaller than the corresponding ones revealed by Fig. 3.

Figure 5c shows the $\alpha(z)$ profile at 355 nm (blue line), 532 nm (green line), and 1064 nm (red line) retrieved from lidar measurements performed on 29 August 2011 from 14:30 to 15:00 UTC. Selected LR values and calculated AOTs are in Table 2. The comparison of Fig. 5c with Fig. 5a reveals both that the aerosol vertical distribution varied within few hours and that the $\alpha(z)$ values retrieved from 14:28 to 15:00 UTC were on average smaller at all wavelengths than the ones retrieved from 11:44 to 12:17 UTC as AOT values also revealed (Table 2). The vertical profiles of $\mathring{a}_{355,532}(z)$, $\mathring{a}_{532,1064}(z)$, $\mathring{a}_{355,1064}(z)$, and $\Delta\mathring{a}(z)$ are plotted in Fig. 5d and we observe

ACPD
13, 18535–18579, 2013

that $\mathring{a}_{355,532}(z)$, $\mathring{a}_{532,1064}(z)$, and $\mathring{a}_{355,1064}(z)$ take nearly equal values at $z > 2$ km a.g.l. Open triangles and error bars in Fig. 6 show the $\Delta\mathring{a}(z)$–$\mathring{a}_{355,1064}(z)$ data points ±1 SD retrieved from the lidar measurements performed within 14:28–15:00 UTC and reveal that the aerosol size distributions were on average characterized by smaller η and larger R_f values at all altitudes, on the afternoon of 29 August. The black open triangles in Fig. 6 represents the columnar values $\Delta\mathring{a}_{in} = 0.20$ and $\mathring{a}_{in}(355, 1064) = 1.4$ which correspond to $\eta_{in} \cong 0.75$ and $R_{f-in} \cong 0.1$ µm. This last result also indicates that the contribution of coarse mode particles slightly increased on the afternoon of 29 August. Figure 7c shows the pathways estimated at 15:00 UTC of the ten day backtrajectories with arrival heights at 1, 2, and 3 km a.g.l. The time evolution of the altitude of each backtrajectory is plotted in Fig. 7d. The air mass origin moved westward at 15:00 UTC and south west Algeria was the source region of the air masses advected at 2 km a.g.l. So, the advection of desert dust particles from Algeria was likely responsible for the smaller η and the larger R_f values (Fig. 6, open triangles) retrieved from the lidar measurements performed on the afternoon of 29 August. The $\mathring{a}_{448,870}$ and $\Delta\mathring{a} = \mathring{a}_{448,675} - \mathring{a}_{675,870}$ values retrieved from the AERONET sunphotometer measurements performed at 11:51 and 14:45 UTC, respectively (Table 2) also indicate that the contribution of coarse mode particles increased on the afternoon of 29 August.

5 Overall results and discussion

The proposed graphical method was applied to lidar measurements performed on several days of the year 2011 to further demonstrate its feasibility and to investigate the dependence on altitude of the fine mode aerosol contribution and of the fine mode aerosol radius. Lidar measurement days were selected in order to have AOTs driven by the main sources characterizing aerosol particles over south eastern Italy. As mentioned, aerosols from continental Europe, the Atlantic and Mediterranean Sea, and the African deserts are frequently advected over south eastern Italy and more generally all over the Central Mediterranean. So, the measurements days that are listed

ACPD
13, 18535–18579, 2013

in Table 2, were representative of the main advection patterns affecting south eastern Italy (Perrone et al., 2013). Selected lidar ratios and calculated AOTs at the lidar wavelengths are given in Table 2, in addition to column-integrated microphysical parameters retrieved from AERONET (Lecce University) sun photometer measurements co-located in time and space with lidar measurements. Table 2 reveals that the investigated measurements days were characterized by AOTs spanning the 0.23–0.53, 0.15–0.41, and 0.04–0.25 range at 355, 532, and 1064 nm, respectively. Lidar ratios varied within the 28–80, 30–70, and 30–55 sr range at 355, 532, and 1064 nm, respectively. Lidar ratio values depend on the aerosol optical and microphysical properties and are commonly used to distinguish aerosol of different types or origin by means of lidar measurements. Coarse non absorbing aerosols such as sea-salt particles are characterized by small lidar ratio values (e.g. Barnaba et al., 2004). Conversely, fine absorbing particles such as soot are characterized by large lidar ratio values (e.g. Barnaba et al., 2007). Thus, measurements days affected by different aerosol types or sources were selected in accordance with aerosol parameters reported in Table 2. Figure 8 shows the scatterplot of LR versus the AOT at 355 nm (dots), 532 nm (triangles), and 1064 nm (boxes), respectively. It is interesting to note that LR values are not correlated to AOTs as it has commonly been found. This result indicates that AOTs are mainly driven by the concentration of aerosols of different optical and microphysical properties. Columnar AERONET parameters retrieved from sunphotometer measurements co-located in space and time with lidar measurements (Table 2) reveal that the AOT and the fine mode fraction η at 675 nm, the Ångstrom coefficient $å_{440,870}$, and the spectral curvature $\Delta å = å_{440,675} - å_{675,870}$ spanned the 0.07–0.34, 0.26–0.83, 0.42–1.84, and −0.09–0.37 range, respectively during the measurement days. The fine mode median radius varied within the 0.126–0.187 µm range. The high variability range of η, $å_{440,870}$, and $\Delta å$ values also indicate that aerosols characterized by different size distributions and hence of different type were monitored on the selected measurement days. Figure 9 shows η(675 nm) and $å_{440,870}$ versus the AOT at 675 nm by dots and triangles, respectively. We observe that η and $å_{440,870}$ do not reveal any marked dependence on the AOT:

ACPD
13, 18535–18579, 2013

fine-mode- ($\eta > 0.6$, $\mathring{a}_{440,870} > 1.4$) and/or coarse-mode ($\eta < 0.4$, $\mathring{a}_{440,870} < 0.8$) dominated aerosols were responsible for high and low AOTs during the measurement days, in accordance with the results revealed by Fig. 8.

Open dots in Fig. 10 show the scatterplot of $\Delta\mathring{a}(z) = \mathring{a}_{355,532}(z) - \mathring{a}_{532,1064}(z)$ versus $\mathring{a}_{355,1064}(z)$ retrieved from the lidar measurements performed on the 11 measurement days. Error bars have not been plotted to make the figure clearer. Different colours were used to represent different measurement days as indicated on the top of Fig. 10. $\mathring{a}(z)$ and $\Delta\mathring{a}(z)$ values retrieved from lidar measurements ranged between 0.12–2.5 and −0.1–0.87, respectively. Figure 11a shows the $\mathring{a}_{355,1064}(z)$ frequency of occurrence plot which was characterized by a bimodal distribution with a main peak at about 1.6 and a secondary peak at about 0.3 mainly due to the contribution of coarse mode particles from the African deserts and/or the Atlantic and Mediterranean Sea (Barnaba et al., 2004; Perrone and Bergamo, 2011). It is interesting to observe that the analysis of one year of AERONET sunphotometer measurements also provided a frequency of occurrence for $\mathring{a}_{440,870}$ rather similar to the one of Fig. 11a (Perrone et al., 2005). The $\Delta\mathring{a}(z)$ frequency of occurrence plot (Fig. 11b) is rather broad with the mean value equal to 0.10 and the standard deviation equal to ±0.4. $\mathring{a}$–$\Delta\mathring{a}$ data points correspond to η and R_f values spanning the 0.30–0.99 and 0.02–0.30 µm range, respectively. The $\eta(z)$ variability range reveals the effect of two separate modes with a significant coarse mode contribution. The spread of the $\mathring{a}$–$\Delta\mathring{a}$ data points allows identifying two main clusters. One cluster represents 17 % of the data points and it is associated to η and R_f values varying within the 30–70 % and 0.07–0.30 µm range, respectively. Four of the 11 measurement days contributed to this cluster where the contribution of coarse mode particles increases as η decreases. 72 % of the data points lie in the cluster delimited by the η curves equal to 70 and 95 %, respectively and the R_f curves equal to 0.05 and 0.15 µm, respectively (Fig. 10). Fine mode particles are dominant in this last cluster and the high percentage of data points indicates that the contribution of fine mode particles was prevailing at the monitoring site of this study. Data points from most of the measurement days contributed to this cluster. This last result indicates that the contribution

ACPD
13, 18535–18579, 2013

of fine mode particles was significant during almost all measurement days. These last results are supported by several studies performed by some of the authors of this paper (e.g. De Tomasi et al., 2006; Tafuro et al., 2007; Santese et al., 2008; Perrone et al., 2013) which revealed that the aerosol load over south eastern Italy is significantly affected by fine pollution aerosols also due to long-range transported contributions from the surrounding populated regions. In particular, the analysis of more than one year of AERONET sunphotometer measurements revealed that the aerosol volume size distribution was bimodal and that the volume (and mass) of aerosols smaller than 1 µm in maximum dimension (fine mode) was dominant during all year, particularly during spring and summer (Tafuro et al., 2007). However, the bimodal structure of the spectrum indicated that along with fine mode particles, which were mainly of anthropogenic origin, coarse mode particles as those of natural (marine and crustal) origin also contributed to the aerosol load during all year. Note that the results revealed by Fig. 10 are in satisfactory agreement with those reported by Basart et al. (2009) which depicted the dominance of fine mode aerosols in driving the AOT at the monitoring site of this study. Quality-assured direct-sun observations of the Lecce University AERONET station, which included 2003–2007 annual cycles, were analyzed by Basart et al. (2009).

Figure 10 shows that the increase of $\mathring{a}$ along constant η curves is associated to the decrease of R_f. On the contrary, the decrease of $\mathring{a}$ along constant R_f curves is associated to the decrease of η and hence, to the larger contribution of coarse mode particles. 5 September 2011 was the day most affected by the contribution of coarse mode particles, in accordance with Fig. 10. Most of the data points lie in the $\Delta\mathring{a}$–$\mathring{a}$ space associated to η and R_f values varying within the 30–50 % and 0.10–0.15 µm range. Figure 12a shows the extinction coefficient vertical profiles at 355, 532, and 1064 nm, respectively and the volume depolarization profile retrieved from the lidar measurements performed on 5 September 2011 from 14:14 to 14:45 UTC. Aerosol particles up to ~ 4 km a.g.l. were detected by the lidar and $\delta(z)$ reached the peak value of 5 % at ~ 3 km a.g.l. Air masses from north-west Africa were mainly advected over south eastern Italy on 5 September 2011, in accordance with the HYSPLIT analytical

ACPD
13, 18535–18579, 2013

backtrajectories (Fig. 13a, b). The BSC-DREAM model also supports the advection of Saharan dust particles. It simulated for the monitoring site of this study, the existence of a dust layer from the ground up to ∼ 4 km at 12:00 UTC (Fig. 12b) and the dust concentrations reached the largest values between 3.0–3.5 km a.g.l., in good accordance with lidar measurements. Hence, both the HYSPLIT analytical backtrajectories and the BSC-DREAM model support the η and R_f values retrieved by the graphical framework of Fig. 10 for 5 September 2011. AERONET sunphotometer measurements also support the results revealed by Fig. 10: η(675 nm) and $\mathring{a}_{448,870}$ reached the smallest values on 5 September 2011 (Table 2). It is also interesting to note from Fig. 10 that R_f spanned the 0.10–0.15 µm range and that $R_{f-in} \cong 0.13$ µm, in satisfactory agreement with the value retrieved from AERONET sunphotometer measurements (Table 2). 3 October 2011 was the day most affected by the contribution of fine mode particles. In fact, Fig. 10 reveals that η and R_f spanned the 90–99 % and 0.07–0.13 µm range, respectively. The AERONET aerosol products support these last results. In fact, Table 2 reveals that η(675 nm) and $\mathring{a}_{448,870}$ reached the largest values on 3 October 2013. These last results further more support the robustness of the proposed graphical approach and reveal the ability of the proposed method to infer the dependence on altitude of the aerosol properties.

Open boxes show $\Delta\mathring{a}_{in}$ versus $\mathring{a}_{in}$ values calculated from the AOTs at 355, 532, and 1064 nm (Eqs. 4 and 5). Figure 10 reveals that the $\Delta\mathring{a}_{in}$–$\mathring{a}_{in}$ data points (open boxes) lie mainly in the space delimited by the η curves equal to 30 and 90 %, respectively and the R_f curves equal to 0.10 and 0.15 µm, respectively. η_{in} and R_{f-in} are in satisfactory agreement with the corresponding η and R_f values retrieved from the AERONET sunphotometer measurements co-located in time and space (Table 2).

We have plotted in Fig. 14 the $\mathring{a}(z)$–$\Delta\mathring{a}(z)$ data points by using different colors to represent data referring to different altitudes a.g.l., in order to investigate the dependence on altitude of η and R_f values and hence, of the aerosol size distribution. The colour bar is on the top of the figure. Figure 14 does not reveal any significant dependence of $\eta(z)$ and $R_f(z)$ on the altitude, at least for the analyzed measurement days. In fact,

ACPD
13, 18535–18579, 2013

the study-cases analysis has clearly revealed that fine particles due to anthropogenic pollution and coarse particles of natural or anthropogenic origin could be found at any altitude sounded by the lidar. Data points retrieved from 1 up to ~ 5 km a.g.l. contributed to both the cluster delimited by the 70–90 %-curves and the 0.05–0.10 m R_f-curves, respectively, where fine mode particles were prevailing, and the cluster delimited by the 30–70 % η curves and the 0.10–0.20 µm R_f curves, respectively where the contribution of coarse mode particles was largest. The advection over south eastern Italy of aerosol from Continental Europe, the Atlantic and the Mediterreanan Sea, and northern Africa contributed to these results, as mentioned.

6 Summary and conclusion

The graphical method of Gobbi and co-authors has for the first time been used to track the changes with altitude of the aerosol properties from 3-wavelength lidar profiles. The method relies on the combined analysis of the Ångstrom coefficient $\mathring{a}_{355,1064}(z)$ and its spectral curvature $\Delta\mathring{a}(z) = \mathring{a}_{355,532}(z) - \mathring{a}_{532,1064}(z)$ which were calculated from the lidar extinction profiles at 355, 532, and 1064 nm, respectively. Plotting data in the $\Delta\mathring{a}(z)$ versus $\mathring{a}_{355,1064}(z)$ coordinates was shown to allow determining the aerosol fine mode radius $R_f(z)$ and fine mode fraction $\eta(z)$ at different altitudes z. Lidar measurements performed on several days of the year 2011 were analyzed to demonstrate the method feasibility. The measurement days were selected in order to have AOTs driven by the main sources of aerosol particles over south eastern Italy. Aerosols from continental Europe, the Atlantic and Mediterranean Sea, and the African deserts are frequently advected over south eastern Italy and more generally all over the Central Mediterranean. As a consequence, aerosol types and hence, $R_f(z)$ and $\eta(z)$ may significantly vary with the altitude over south eastern Italy. Volume depolarization ratio profiles from lidar measurements, HYSPLIT analytical backtrajectories, the BSC-DREAM model, MODIS satellite images, and AERONET (Lecce University) sunphotometer measurements collocated in space and time with lidar measurements were used to understand and sup-

ACPD
13, 18535–18579, 2013

port the dependence on z of R_f and η values retrieved from the proposed graphical method for different measurement days. Paper's results have demonstrated that:

a. $\eta(z)$ and $R_f(z)$ varied within the 0.30–0.99 and 0.02–0.30 µm range, respectively at the monitoring site of this study, and that

b. $R_f(z)$ and $\eta(z)$ varied significantly with altitude mainly when aerosol of different type and hence from different sources were at different altitudes a.g.l.

c. It was found that $R_f(z)$ and $\eta(z)$ were not dependent on the altitude from the ground level: fine particles due to anthropogenic pollution and coarse particles of natural or anthropogenic origin could be found at any altitude sounded by the lidar.

d. Results depicted the dominance of fine mode aerosols in driving the AOT over south eastern Italy: 72 % of the $R_f(z)$ and $\eta(z)$ values were within the 0.05–0.15 µm and 0.70–0.95 range, respectively. However, the $\eta(z)$ variability which spanned the 0.30–0.99 range has indicated that along with fine mode particles, coarse mode particles as those of natural (marine and crustal) origin also contributed to the aerosol load during all measurement days.

In conclusion, the results of this study have shown the robustness of the proposed graphical approach to infer $R_f(z)$ and $\eta(z)$ values from 3-wavelength lidar measurements. Then, the high variability of R_f and η with z has demonstrated the importance of accounting for the dependence on z of the aerosol size distribution. We believe that the results on $R_f(z)$ and $\eta(z)$ combined with the column-integrated size distributions retrieved from AERONET sunphotometer measurements collocated in space and time with lidar measurements, should allow obtaining particle size distributions dependent on z by a closure analysis. Work is on progress in this direction. It is worth noting that the monitoring site of this study is on a flat peninsula of south eastern Italy, more than 40 km away from large industrial sites. As a consequence, it can be considered representative of the aerosol load affecting the Central Mediterranean. Hence, paper's

ACPD
13, 18535–18579, 2013

results have also highlighted some of the main features of the aerosol particles affecting the Central Mediterranean and have revealed the importance of accounting for altitude-dependent size distributions in radiative transfer simulations.

Acknowledgements. This study was supported by the European Community through the ACTRIS Research Infrastructure Action under the 7th Framework Programme under ACTRIS Grant Agreement no. 262254. The authors would also like to acknowledge NASA/Goddard Space Flight Center and the Barcelona Super-Computing Centre for their contribution with satellite images, and DREAM dust profiles, respectively. The authors gratefully acknowledge the NOAA Air Resources Laboratory (ARL) for the provision of the HYSPLIT backtrajectories used in this publication. The authors gratefully acknowledge O. Cavalieri for carrying out some measurements and contributing to some data analysis.

References

Barnaba, F., De Tomasi, F., Gobbi, G. P., Perrone, M. R., and Tafuro, A.: Extinction versus backscatter relationships for lidar applications at 351 nm: maritime and desert aerosol simulations and comparison with observations, Atmos. Res., 70, 229–259, 2004.

Barnaba, F., Tafuro, A. M., De Tomasi, F., and Perrone, M. R.: Observed and simulated vertically resolved optical properties of continental aerosols over southeastern Italy: a closure study, J. Geophys. Res., 112, D10203, doi:10.1029/2006JD007926, 2007.

Basart, S., Pérez, C., Cuevas, E., Baldasano, J. M., and Gobbi, G. P.: Aerosol characterization in Northern Africa, Northeastern Atlantic, Mediterranean Basin and Middle East from direct-sun AERONET observations, Atmos. Chem. Phys., 9, 8265–8282, doi:10.5194/acp-9-8265-2009, 2009.

Chaikovsky, A., Dubovik, O., Goloub, P., Tanre, D., Pappalardo, G., Wandinger, U., Chaikovskaya, L., Denisov, S., Grudo, Y., Lopatsin, A., Karol, J., Lapyonok, T., Korol, M., Osipenko, F., Savitski, D., Slesar, A., Apituley, A., Alados Arboledas, L., Binietoglou, I., Kokkalis, P., Granados Munoz, M. J., Papayannis, A., Perrone, M. R., Pietruczuk, A., Pisani, G., Rocadenbosch, F., Sicard, M., De Tomasi, F., Wagner, J., and Wang, X.: Algorithm and software for the retrieval of vertical aerosol properties using combined lidar/radiometer data: dissemination in EARLINET, Reviewed and Revised Papers of the 26th International Laser Radar Conference, 25–29 June, Porto Heli, Greece, Paper SO3-09, 2012.

ACPD
13, 18535–18579, 2013

Cavalieri, O., Perrone, M. R., De Tomasi, F., and Gobbi, G. P.: Three wavelengths lidar measurements for atmospheric aerosol characterization, Reviewed and Revised Papers of the 26th International Laser Radar Conference, 25–29 June, Porto Heli, Greece, Paper SO3-09, 2012.

De Tomasi, F. and Perrone, M. R.: Lidar measurements of tropospheric water vapor and aerosol profiles over southeastern Italy, J. Geophys. Res., 108, 4286–4297, 2003.

De Tomasi, F. and Perrone, M. R.: PBL and dust layer seasonal evolution by lidar and radiosounding measurements over a peninsular site, Atmos. Res., 80, 86–103, 2006.

De Tomasi, F., Blanco, A., and Perrone, M. R.: Raman lidar monitoring of extinction and backscattering of African dust layers and dust characterization, Appl. Optics, 42, 1699–1709, 2003.

De Tomasi, F., Tafuro, A. M., and Perrone, M. R.: Height and seasonal dependence of aerosol optical properties over southeast Italy, J. Geophys. Res., 111, D10203, doi:10.1029/2005JD006779, 2006.

De Tomasi, F., Miglietta, M., and Perrone, M. R.: The growth of the planetary boundary layer at a coastal site: a case study, Bound.-Lay. Meteorol., 139, 521–541, doi:10.1007/s10546-011-9592-6, 2011.

Draxler, R. R. and Rolph, G. D.: HYSPLIT (HYbrid Single-Particle Lagrangian Integrated Trajectory) model, available at: http://www.arl.noaa.gov/ready/hysplit4.html (last access: May 2013), NOAA Air Resources Laboratory, Silver Spring, MD, 2003.

Dubovik, O., Holben, B. N., Lapyonok, T., Sinyuk, A., Mishchenko, M. I., Yang, P., and Slutsker, I.: Non-spherical aerosol retrieval method employing light scattering by spheroids, Geophys. Res. Lett. 29, 1415, doi:10.1029/2001GL014506, 2002.

Gobbi, G. P., Kaufman, Y. J., Koren, I., and Eck, T. F.: Classification of aerosol properties derived from AERONET direct sun data, Atmos. Chem. Phys., 7, 453–458, doi:10.5194/acp-7-453-2007, 2007.

Gross, S., Tesche, M., Freudenthaler, V., Toledano, C., Wiegner, M., Ansmann, A., Althausen, D., and Seefeldner, M.: Characterization of Sahara dust, marine aerosols and mixtures of biomass-burning aerosols and dust by means of multi-wavelength depolarization and Raman lidar Measurements during SAMUN 2, Tellus B, 63, 706–724, 2011.

Holben, B. N., Eck, T. F., Slutsker, I., Tanré, D., Buis, J. P., Setzer, A., Vermote, E., Reagan, J. A., Kaufman, Y. J., Nakajima, T., Lavenu, F., Jankowiak, I., and Smirnov, A.: AERONET – a feder-

ACPD
13, 18535–18579, 2013

ate instrument network and data archive for aerosol characterization, Remote Sens. Environ., 66, 1–16, 1998.
Kaufman, Y. J.: Aerosol optical thickness and atmospheric path radiance, J. Geophys. Res., 98, 2677–2692, 1993.
Kolgotin, A. and Muller, D.: Theory of inversion with two-dimensional regularization: profiles of microphysical particle properties derived from multiwavelength lidar measurements, Appl. Optics, 47, 4472–4490, 2008.
Lelieveld, J., Berresheim, H., Borrmann, S., Crutzen, P. J., Dentener, F. J., Fischer, H., Feichter, J., Flatau, P. J., Heland, J., Holzinger, R., Korrmann, R., Lawrence, M. G., Levin, Z., Markowicz, K. M., Mihalopoulos, N., Minikin, A., Ramanathan, V., de Reus, M., Roelofs, G. J., Scheeren, H. A., Sciare, J., Schlager, H., Schultz, M., Siegmund, P., Steil, B., Stephanou, E. G., Stier, P., Traub, M., Warneke, C., Williams, J., and Ziereis, H.: Global air pollution crossroads over the Mediterranean, Science, 298, 794–799, 2002.
Matthias, V., Freudenthaler, V., Amodeo, A., Balis, D., Boesenberg, J., Chaikovsky, A., Chourdakis, G., Comeron, A., Delaval, A., De Tomasi, F., Eixmann, R., Hagard, A., Komguem, L., Kreipl, S., Matthey, R., Rizi, V., Rodrigues, J. A., Wandinger, U., and Wang, X.: Aerosol lidar intercomparison in the framework of the EARLINET project: 1. Instrument, Appl. Optics, 43, 961–976, 2004.
Pahlow, M., Muller, D., Tesche, M., Eichler, H., Feingold, G., Eberhard, W., L., and Cheng, Y.: Retrieval of aerosol properties from combined multiwavelength lidar and sunphotometer measurements, Appl. Optics, 45, 7429–7442, 2006.
Perrone, M. R. and Bergamo, A.: Direct radiative forcing during Sahara dust intrusions at a site in the Central Mediterranean: anthropogenic particle contribution, Atmos. Res., 101, 783–798, 2011.
Perrone, M. R., Santese, M., Tafuro, A. M., Holben, B., and Smirnov, A.: Aerosol load characterization over South-East Italy for one year of AERONET sun-photometer measurements, Atmos. Res., 75, 111–133, 2005.
Perrone, M. R., Tafuro, A. M., and Kinne, S.: Dust layer effects on the atmospheric radiative budget and heating rate profiles, Atmos. Environ., 59, 344–354, 2012.
Perrone, M. R., Becagli, S., Orza, J. A. G., Vecchi, R., Dinoi, A., Udisti, R., and Cabello, M.: The impact of long-range-transport on PM_1 and $PM_{2.5}$ at a Central Mediterranean site, Atmos. Environ., 71, 176–186, 2013.

ACPD
13, 18535–18579, 2013

Santese, M., De Tomasi, F., and Perrone, M. R.: Advection patterns and aerosol optical and microphysical properties by AERONET over south-east Italy in the central Mediterranean, Atmos. Chem. Phys., 8, 1881–1896, doi:10.5194/acp-8-1881-2008, 2008.
Seinfeld, J. H. and Pandis, S. N.: Atmospheric Chemistry and Physics: from Air Pollution to Climate Change, J. Wiley & Sons inc., 1998.
Schuster, G. L., Dubovick, O., and Holben, B. N.: Ångstrom exponent and bimodal aerosol size distributions, J. Geophys. Res., 111, D07207, doi:10.1029/2005JD006328, 2006.
Tafuro, A. M., Kinne, S., De Tomasi, F., and Perrone, M. R.: Annual cycle of aerosol direct radiative effect over southeast Italy and sensitivity studies, J. Geophys. Res., 112, D20202, doi:10.1029/2006JD008265, 2007.
Tesche, M., Asman, A., Müller D., Althausen, D., Engelmann, R., Freudenthaler, V., and Groß, S.: Vertically resolved separation of dust and smoke over Cape Verde using multi-wavelength Raman and polarization lidars during Sahara Mineral Dust Experiment 2008, J. Geophys. Res., 114, D13202, doi:10.1029/2009JD011862, 2009.
Veselovskii, I., Kolgotin, A., Griaznov, V., Muller, D., Wandinger, U., and Whiteman, D.: Inversion with regularization for the retrieval of tropospheric aerosol parameters from multi-wavelength lidar sounding, Appl. Optics, 41, 3685–3699, 2002.
Veselovskii, I., Dubovik, O., Kolgotin, A., Korenskiy, M., Whiteman, D. N., Allakhverdiev, K., and Huseyinoglu, F.: Linear estimation of particle bulk parameters from multi-wavelength lidar measurements, Atmos. Meas. Tech., 5, 1135–1145, doi:10.5194/amt-5-1135-2012, 2012.

ACPD
13, 18535–18579, 2013

Table 1. Real (n) and imaginary (k) refractive index values at 532 nm used in the Mie simulations for mixed aerosol loads and for aerosol loads significantly affected by desert dust intrusions (n_c, k_c) and continental pollution (n_f, k_f).

Aerosol type		
Mixed aerosol (n, k)	1.455	0.0047
Dust affected (n_c, k_c)	1.483	0.0035
Pollution affected (n_f, k_f)	1.445	0.0070

ACPD
13, 18535–18579, 2013

Table 2. Lidar Ratios (LR) and AOTs at the laser wavelengths. Measurement day and time interval (T_1–T_2 (UTC)) during which lidar measurements were performed are also provided. The fine mode fraction (η) at 675 nm, the fine mode median radius (R_f), $\mathring{a}_{448,870}$, and $\Delta\mathring{a} = \mathring{a}_{448,675} - \mathring{a}_{675,870}$ values retrieved from the AERONET sunphotometer measurements performed at the time T_A (UTC) are also given.

Lidar Aerosol Product							AERONET Aerosol Products					
Day yy/mm/dd (T_1–T_2)	LR (sr) (wavelengths, nm) 355	532	1064	AOT (wavelengths, nm) 355	532	1064	T_A hhmm	η at 675 nm	R_f (μm)	$\mathring{a}_{440,870}$	$\Delta\mathring{a}$	AOT at 675 nm
11/04/11 12:34–13:15	55	55	50	0.28	0.23	0.16	12:50	0.30	0.15	0.42	0.27	0.19
11/05/30 11:59–12:30	50	50	50	0.41	0.24	0.07	09:47	0.78	0.19	1.54	0.04	0.16
11/06/06 11:44–12:15	60	55	55	0.42	0.29	0.17	11:48	0.40	0.16	0.73	0.24	0.25
11/06/09 13:29–13:42	30	30	30	0.34	0.16	0.055	12:48	0.71	0.16	1.55	0.37	0.12
11/06/20 12:44–13:15	45	45	35	0.26	0.15	0.05	12:50	0.64	0.16	1.50	0.35	0.11
11/07/28 12:29–13:00	80	70	50	0.33	0.20	0.06	12:55	0.75	0.17	1.51	−0.09	0.14
11/08/23 11:44–12:15	80	65	55	0.41	0.21	0.06	11:52	0.74	0.13	1.71	0.08	0.14
11/08/29 11:44–12:15	55	50	38	0.67	0.30	0.12	11:51	0.67	0.15	1.54	0.08	0.26
11/08/29 14:28–15:00	55	53	41	0.50	0.29	0.10	14:45	0.65	0.14	1.49	0.20	0.20
11/09/05 14:14–14:45	55	55	55	0.53	0.41	0.25	14:34	0.26	0.13	0.45	0.18	0.34
11/09/29 12:44–13:16	70	70	40	0.23	0.12	0.053	11:40	0.77	0.16	1.40	0.30	0.07
11/10/03 12:41–13:16	70	70	35	0.32	0.15	0.04	13:39	0.83	0.13	1.84	0.22	0.09

ACPD
13, 18535–18579, 2013

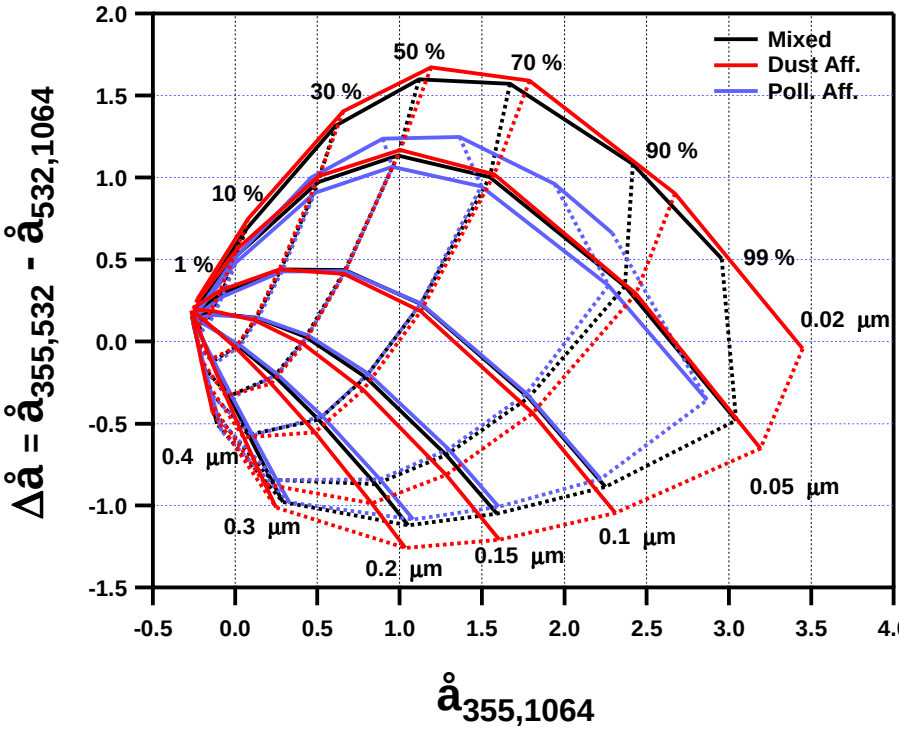

Fig. 1. Graphical framework for the aerosol characterization calculated according to Gobbi et al. (2007) for $n = 1.455$ and $k = 0.0047$ (black lines), $n_c = 1.483$ and $k_c = 0.0035$ (red lines), and $n_f = 1.445$ and $k_f = 0.0070$ (blue lines) at 532 nm.

ACPD
13, 18535–18579, 2013

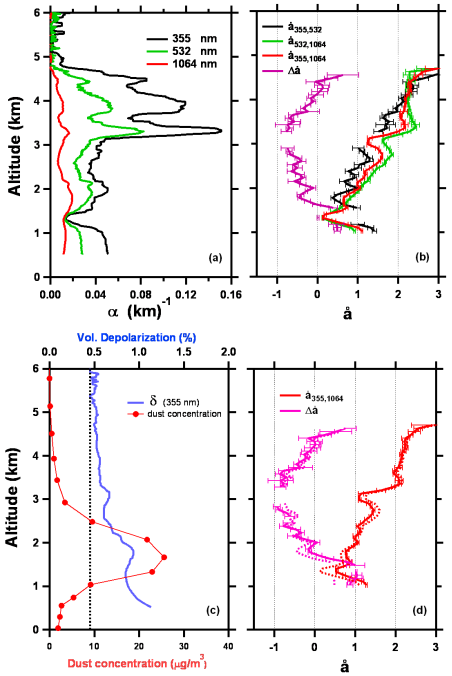

Fig. 2. (a) Extinction coefficient profiles at 355 nm (black line), 532 nm (green line), and 1064 nm (red line) retrieved from lidar measurements performed on 28 July 2011 from 12:29 to 13:00 UTC. **(b)** Vertical profiles of the Ångstrom coefficients $\mathring{a}_{355,532}(z)$, $\mathring{a}_{532,1064}(z)$, $\mathring{a}_{355,1064}(z)$, and of the spectral curvature $\Delta\mathring{a}(z)$. Altitude independent lidar ratio values equal to 80 sr, 70 sr, and 50 sr at 355 nm, 532 nm, and 1064 nm, respectively were used to retrieve the vertical profiles plotted in **(a, b)**. **(c)** Vertical profile of the volume depolarization ratio (blue line) and the dust particle concentration from the BSC-DREAM model (red line). **(d)** Vertical profiles of the Ångstrom coefficients $\mathring{a}_{355,1064}(z)$ and the spectral curvature $\Delta\mathring{a}(z)$ calculated from extinction profiles based on altitude dependent lidar ratio values. Dotted lines represent the corresponding profiles plotted in **(b)**.

ACPD
13, 18535–18579, 2013

Vertically resolved aerosol properties by multi wavelengths lidar measurements

M. R. Perrone et al.

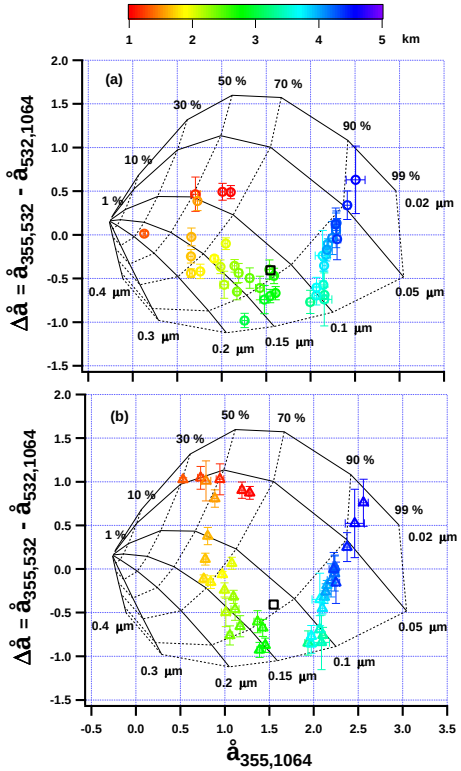

Fig. 3. Solid and dashed black lines represent the graphical framework calculated for $n = 1.455$ and $k = 0.0047$ at 532 nm. **(a)** Open dots represent calculated $\Delta\mathring{a}(z)$ versus $\mathring{a}(z)$ values. Error bars represent ±1 standard deviation (SD) of the mean value. Different colours are used to represent $\Delta\mathring{a}(z)$–$\mathring{a}(z)$ values referring to different z, as indicated by the colour bar on the top of the figure. The full black box represents the columnar $\mathring{a}_{in}(355, 1064)$ and $\Delta\mathring{a}_{in}$ values calculated from Eqs. (4) and (5), respectively. **(b)** Open triangles represent $\Delta\mathring{a}(z)$ versus $\mathring{a}(z)$ values calculated from extinction profiles based on altitude dependent lidar ratio values.

ACPD
13, 18535–18579, 2013

Vertically resolved aerosol properties by multi wavelengths lidar measurements

M. R. Perrone et al.

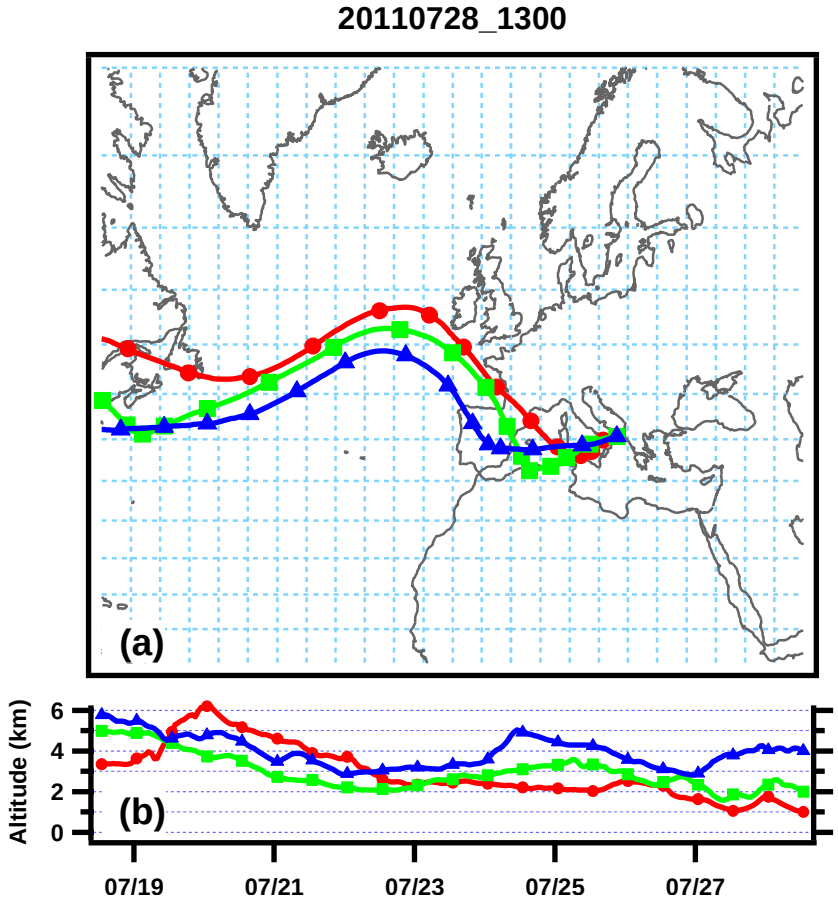

Fig. 4. (a) Pathways estimated at 13:00 UTC of 28 July 2011, of the ten day HYSPLIT backtrajectories with arrival heights at 1, 2, and 4 km a.g.l. **(b)** Time evolution of the altitude of each backtrajectory.

ACPD
13, 18535–18579, 2013

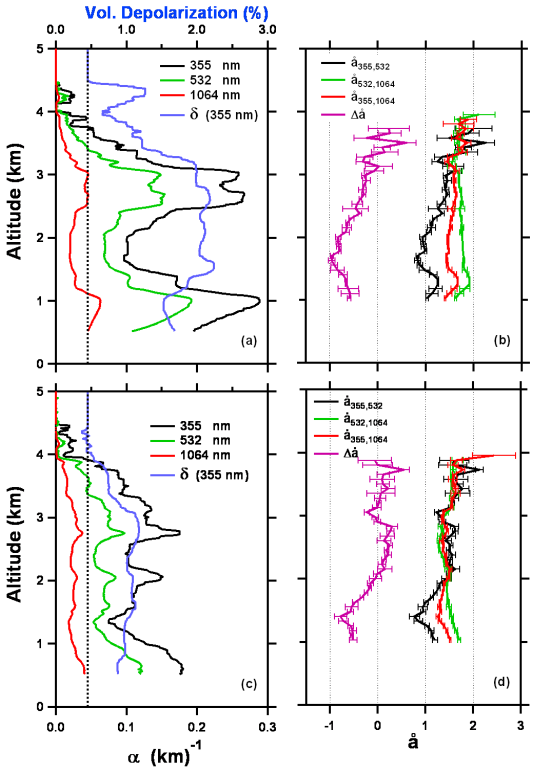

Fig. 5. Extinction coefficient profile at 355 nm (black line), 532 nm (green line), and 1064 nm (red line) retrieved from lidar measurements performed on 29 August 2011 **(a)** from 11:36 to 12:06 UTC and **(c)** from 14:30 to 15:00 UTC. Vertical profiles of the Ångstrom coefficients $\mathring{a}_{355,532}(z)$, $\mathring{a}_{532,1064}(z)$, and $\mathring{a}_{355,1064}(z)$ and of the spectral curvature $\Delta\mathring{a}(z)$ from lidar measurements performed within **(b)** 11:36–12:06 UTC and **(d)** 14:30 to 15:00 UTC. Blue lines represent the volume depolarization ratio vertical profiles.

ACPD
13, 18535–18579, 2013

Vertically resolved aerosol properties by multi wavelengths lidar measurements

M. R. Perrone et al.

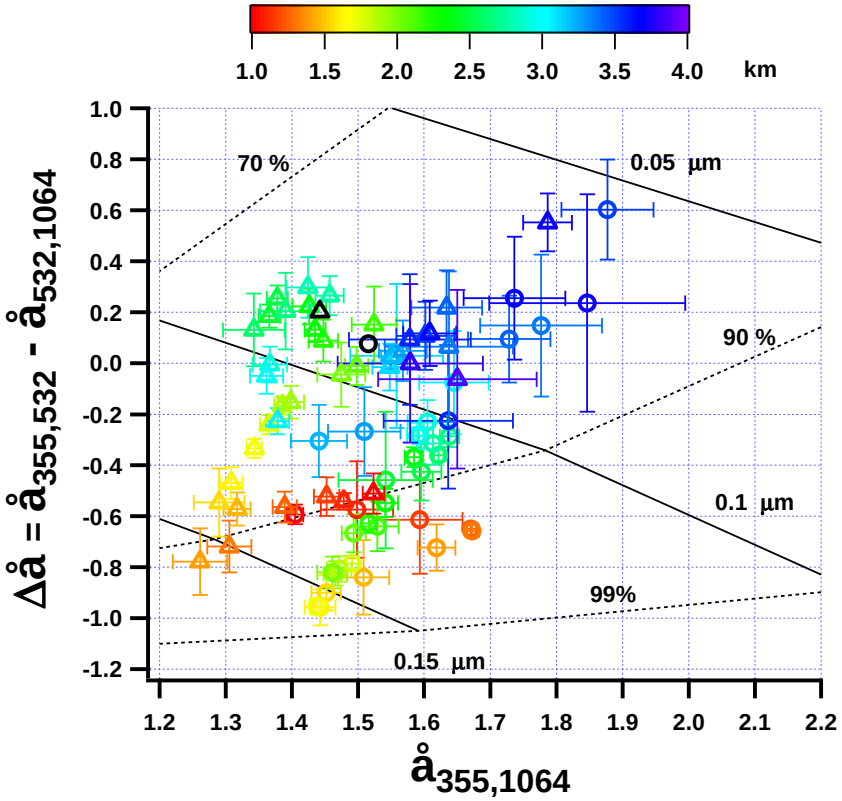

Fig. 6. Scatterplot of $\Delta\mathring{a}(z)$ versus $\mathring{a}_{355,1064}(z)$ retrieved from the lidar measurements performed on 29 August 2011 within 11:36–12:06 UTC (open dots) and 14:30–15:00 UTC (open triangles). Different colours represent different altitudes in accordance with the colour bar on the top. A portion of the graphical framework calculated for $n = 1.455$ and $k = 0.0047$ at 532 nm is reported in the figure. The open black dot and triangle represent the $\Delta\mathring{a}_{in}$ and $\mathring{a}_{in}(355, 1064)$ data points calculated from the lidar measurements performed within 11:36–12:06 UTC and 14:30–15:00 UTC, respectively.

ACPD
13, 18535–18579, 2013

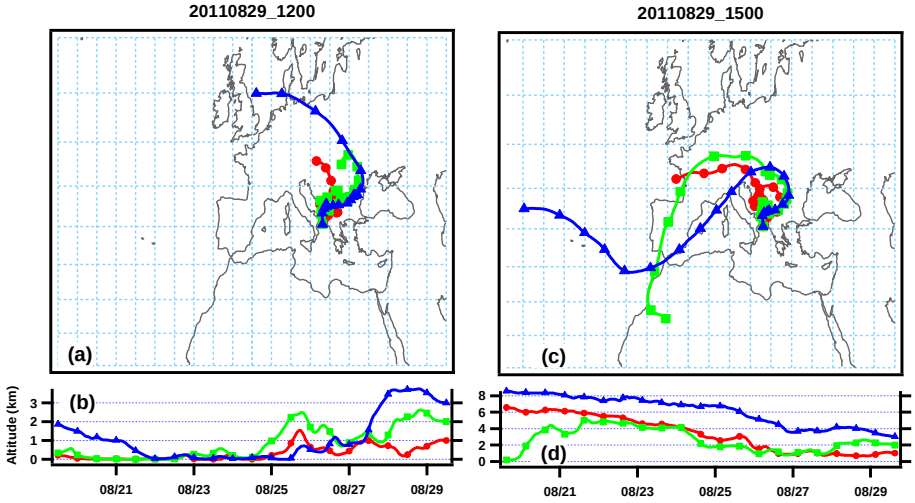

Fig. 7. Pathways of the ten day HYSPLIT backtrajectories of 29 August 2011 estimated **(a)** at 12:00 UTC and **(c)** at 15:00 UTC with arrival heights at 1, 2, and 3 km a.g.l., respectively. Time evolution of the altitude of each backtrajectory estimated at **(b)** 12:00 UTC and **(d)** 15:00 UTC.

ACPD
13, 18535–18579, 2013

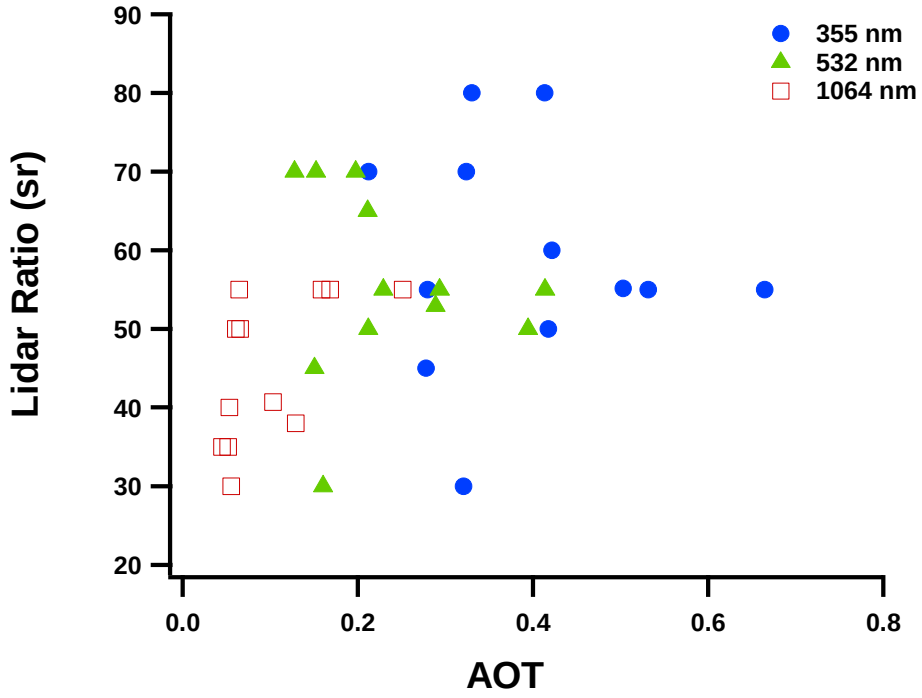

Fig. 8. Scatterplot of LR versus the AOT at 355 nm (dots), 532 nm (triangles), and 1064 nm (boxes), respectively.

ACPD
13, 18535–18579, 2013

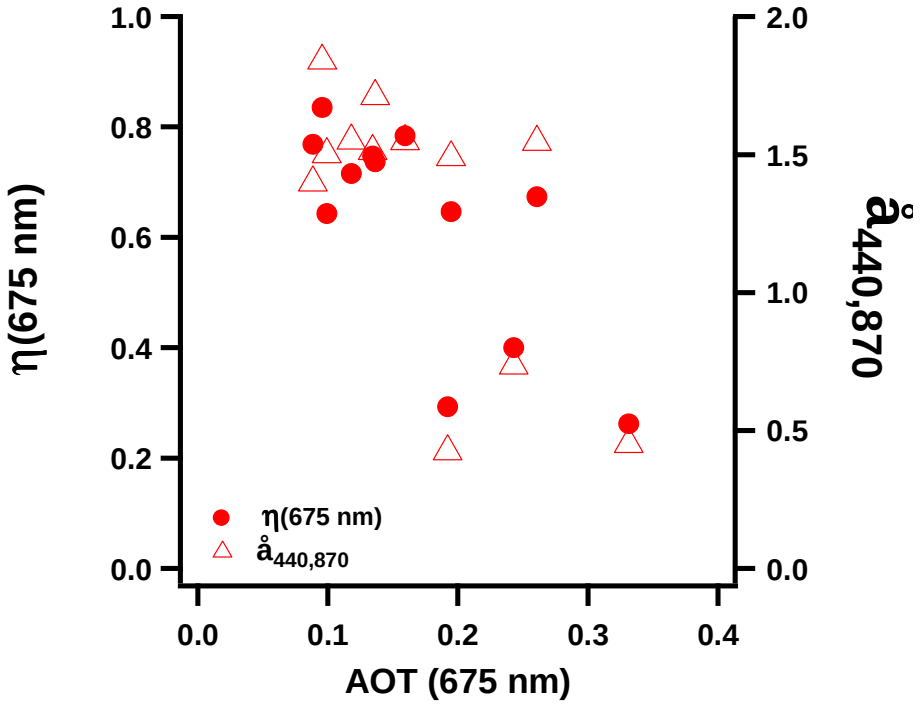

Fig. 9. Scatterplot of η(675 nm) (dots) and $\mathring{a}_{440,870}$ (triangles) versus the AOT(675 nm) retrieved from AERONET sunphotometer measurements co-located in space and time with lidar measurements.

ACPD
13, 18535–18579, 2013

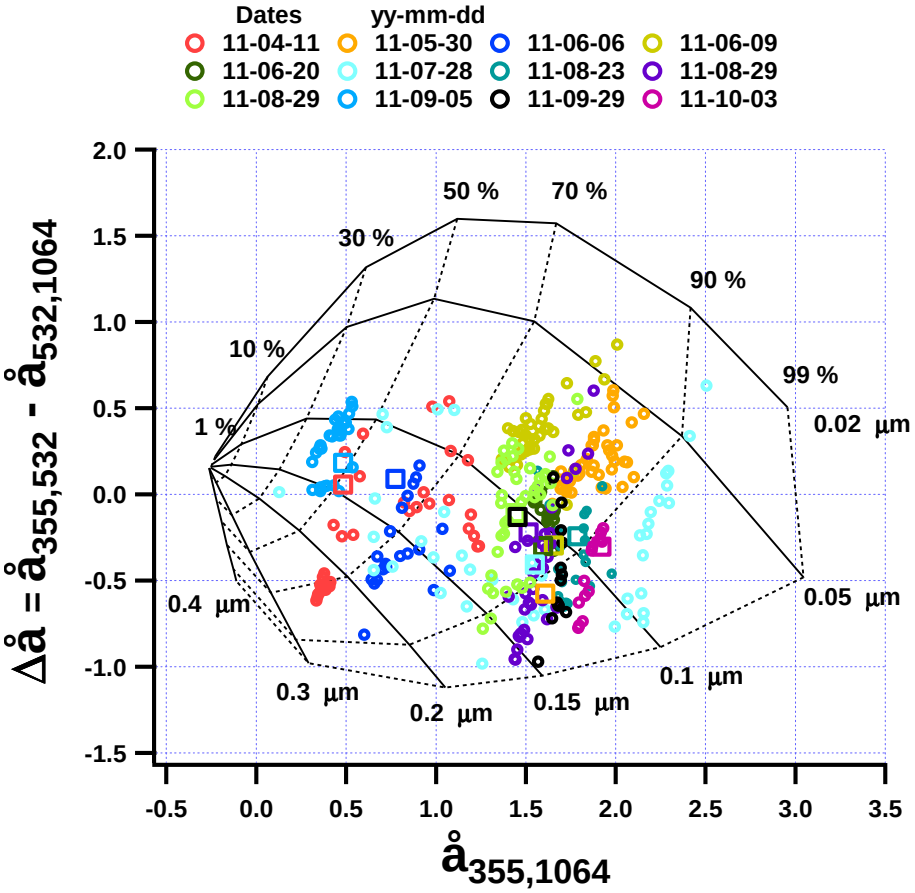

Fig. 10. Scatterplot of $\Delta å(z)$ versus $å_{355,1064}(z)$ retrieved from the lidar measurements performed on eleven measurement days. Different colours are used to represent different measurement days.

ACPD
13, 18535–18579, 2013

Vertically resolved aerosol properties by multi wavelengths lidar measurements

M. R. Perrone et al.

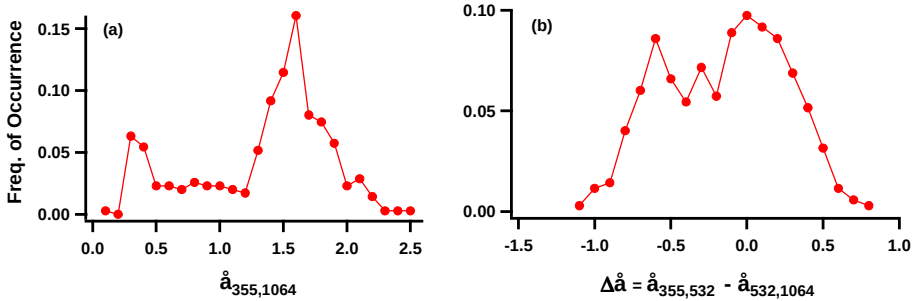

Fig. 11. Frequency of occurrence plot of **(a)** $\mathring{a}_{355,1064}(z)$ and **(b)** $\Delta\mathring{a}(z)$.

ACPD
13, 18535–18579, 2013

Vertically resolved aerosol properties by multi wavelengths lidar measurements

M. R. Perrone et al.

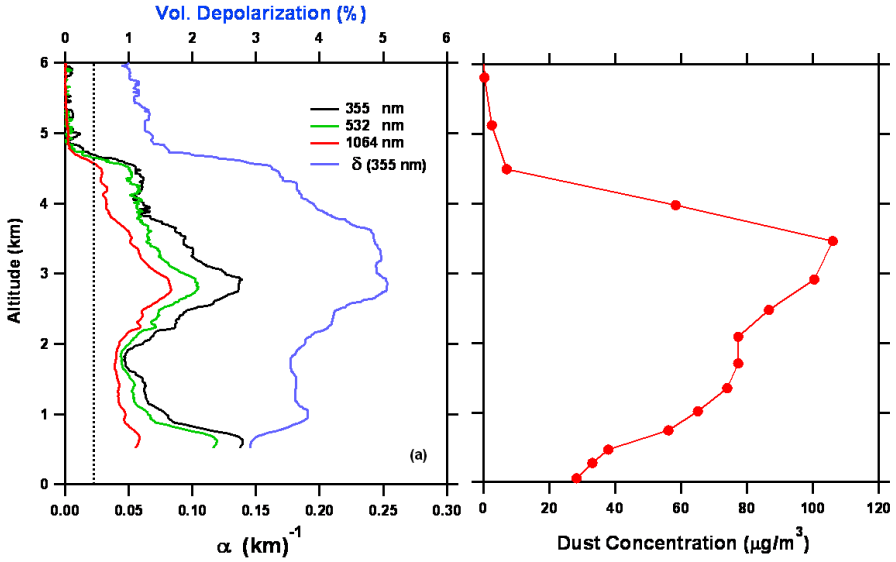

Fig. 12. (a) Extinction coefficient vertical profiles at 355 (black line), 532 (green line), and 1064 nm (red line), respectively and volume depolarization ratio profile (blue line) retrieved from lidar measurements performed on 5 September 2011, from 14:14 to 14:45 UTC. **(b)** Dust particle concentration from the BSC-DREAM model at 12:00 UTC of 5 September 2011.

ACPD
13, 18535–18579, 2013

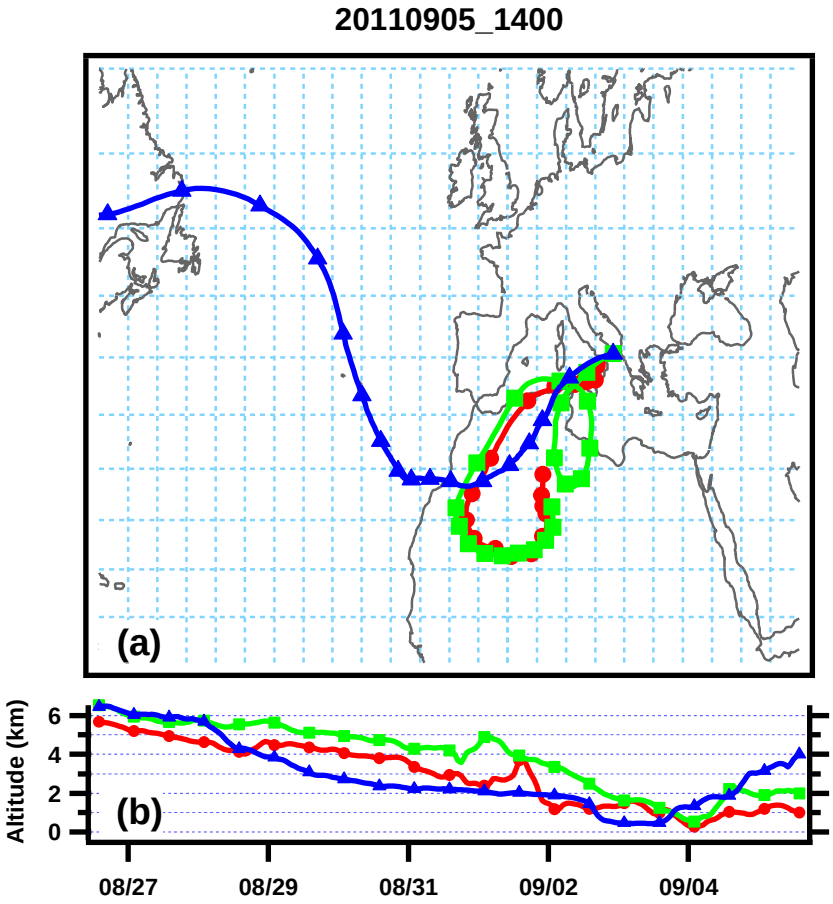

Fig. 13. (a) Pathways estimated at 14:00 UTC of 5 September 2011 of the ten day HYSPLIT backtrajectories with arrival heights at 1, 2, and 4 km a.g.l. **(b)** Time evolution of the altitude of each backtrajectory.

ACPD
13, 18535–18579, 2013

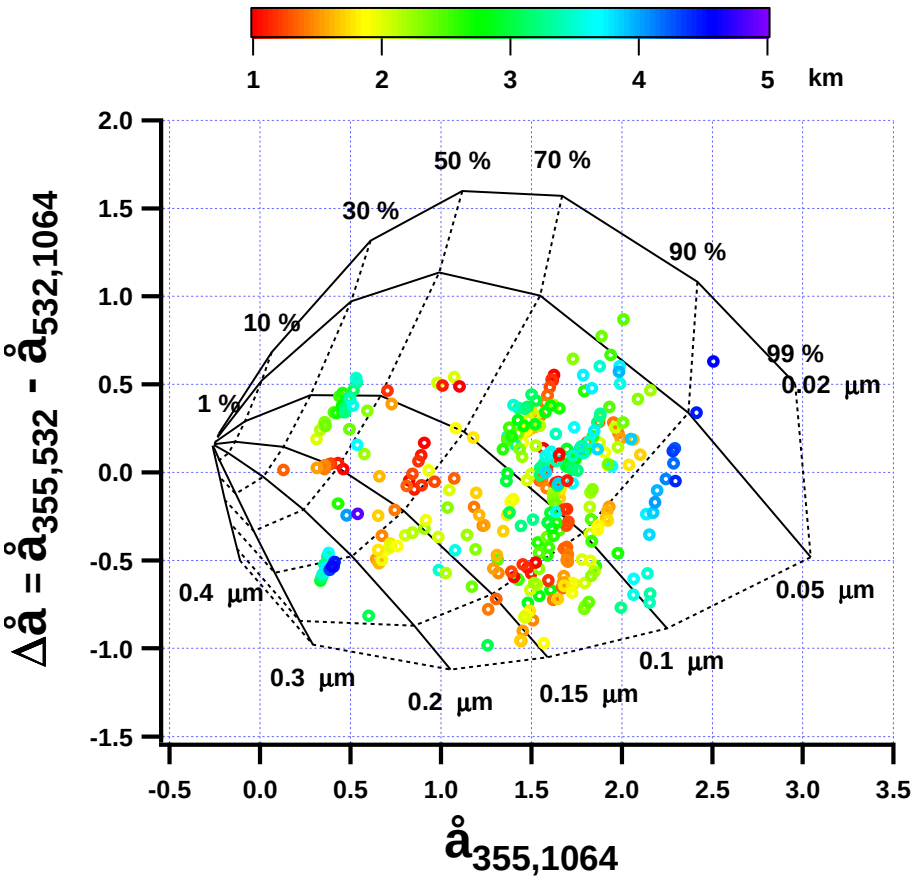

Fig. 14. Scatterplot of $\Delta å(z)$ versus $å_{355,1064}(z)$ retrieved from the lidar measurements performed on 11 measurement days. Different colours are used to represent different altitudes a.g.l.

ACPD
13, 18535–18579, 2013

Vertically resolved aerosol properties by multi wavelengths lidar measurements

M. R. Perrone et al.